Hyperspectral tomography based on multi-mode absorption spectroscopy (MUMAS)

Jinghang Dai, Seamus O'Hagan, Hecong Liu, Weiwei Cai, and Paul Ewart

Citation: Appl. Phys. Lett. **111**, 184102 (2017);
View online: https://doi.org/10.1063/1.5002888
View Table of Contents: http://aip.scitation.org/toc/apl/111/18
Published by the American Institute of Physics

Hyperspectral tomography based on multi-mode absorption spectroscopy (MUMAS)

Jinghang Dai,[1] Seamus O'Hagan,[2] Hecong Liu,[1] Weiwei Cai,[1,a)] and Paul Ewart[2]
[1]*Department of Mechanical Engineering, Shanghai Jiao Tong University, Shanghai 200240, China*
[2]*Department of Physics, Clarendon Laboratory, Oxford University, Parks Road, Oxford OX1 3PU, United Kingdom*

(Received 1 September 2017; accepted 11 October 2017; published online 30 October 2017)

This paper demonstrates a hyperspectral tomographic technique that can recover the temperature and concentration field of gas flows based on multi-mode absorption spectroscopy (MUMAS). This method relies on the recently proposed concept of nonlinear tomography, which can take full advantage of the nonlinear dependency of MUMAS signals on temperature and enables 2D spatial resolution of MUMAS which is naturally a line-of-sight technique. The principles of MUMAS and nonlinear tomography, as well as the mathematical formulation of the inversion problem, are introduced. Proof-of-concept numerical demonstrations are presented using representative flame phantoms and assuming typical laser parameters. The results show that faithful reconstruction of temperature distribution is achievable when a signal-to-noise ratio of 20 is assumed. This method can potentially be extended to simultaneously reconstructing distributions of temperature and the concentration of multiple flame species. *Published by AIP Publishing.* https://doi.org/10.1063/1.5002888

Tomographic absorption spectroscopy (TAS) has been evolving into a well-established imaging technique and has found numerous applications in combustion diagnostics.[1] According to the mathematical principle it relies on, TAS can be divided into linear and nonlinear modalities.[2] The linear modality is based on the classical concept of tomography and typically measures the absorbance of the target flow along various directions to record the so-called sinogram, which is then processed to recover the distribution of the absorption coefficient at a specific transition.[3,4] Repeating this process for a second transition, another map of the absorption coefficient can be retrieved. The method of two-line thermometry can then be applied to each single pixel to solve for the local temperature and species concentration.[5] As only two transitions are probed, the linear modality typically requires one or two tunable diode lasers.[6] On the other hand, the nonlinear modality measures a reduced number of projections (typically two orthogonal ones) but with an increased number of transitions.[7] Both time[8] and frequency division[9] multiplexing have been adopted to realize such multispectral measurements. The former category can be implemented using either a Fourier domain mode locking laser (FDML)[10] or a chirped super-continuum.[8] The latter category can be realized using multiple tunable diode lasers,[9] each modulated at a distinct frequency and targeted at a distinct individual transition. The absorption signals for the transitions can then be separated using lock-in amplifiers. In both approaches, the absorption signals are spectrally resolved and used as the inputs for the nonlinear tomographic reconstruction. In this work, we adopt an alternative way of wavelength multiplexing for the implementation of nonlinear TAS. This approach is based on the so-called multi-mode absorption spectroscopy (MUMAS), which was first demonstrated in 2005 using a multi-mode tunable diode laser.[11] Since then, this method has been further demonstrated using a variety of multi-mode lasers including micro-lasers,[12] quantum cascade lasers,[13] and interband cascade lasers.[14,15] In contrast to the previous implementations of absorption tomography, MUMAS does not rely on individual spectrally resolved absorption signals.[16] Rather, it provides a signal, the MUMAS signature, which is characteristic of the multimode laser spectrum and a set of spectral features determined by the absorbing species.[17] When the laser mode parameters are known together with the relevant spectral information on the absorbing species, the recorded MUMAS signature or spectrum can be used to derive temperature, pressure, and individual species concentrations averaged over the line-of-sight.[18] Such a detection strategy provides some advantages: a broadband multi-mode laser can be used, which simultaneously probes multiple flame species, and such sources are readily available from the visible to mid-infrared range which covers the absorption bands of both major and minor flame species. Furthermore, it is cost-effective when compared with the broadband light sources such as the FDML and supercontinuum radiation. These features suggest the possibility of a tomographic modality based on MUMAS.

MUMAS is a spectroscopic technique, whereby the radiation from each mode of a certain laser comb interacts with the molecular absorption transitions of a target gas.[19] While the modes are scanned simultaneously across a frequency range of ν_{scan}, the transmission spectrum of the ith sampling beam is recorded as illustrated in Fig. 1. The spectrum is dictated by both the absorption transitions that lie within the overall scanned spectral range and the properties of the laser comb and can be modeled as the weighted summation of the transmitted intensity of all modes as follows:

$$P_i(\nu_{scan}) = \sum_q W_q(\nu_{scan}) \cdot (1 - A_i(\nu)), \tag{1}$$

where q is the mode index, $W_q(\nu_{\text{scan}})$ is the mode fractional power, ν is the absolute frequency, and $A_i(\nu)$ is the absorption

a)Electronic mail: cweiwei@sjtu.edu.cn

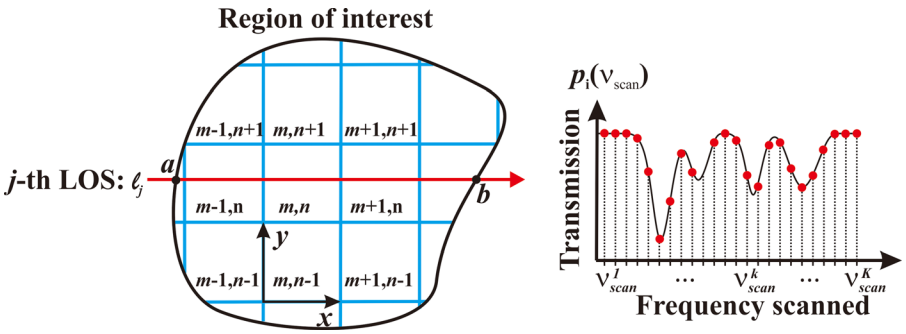

FIG. 1. Mathematical formulation for tomographic MUMAS.

spectrum of the ith beam, which can be calculated according to the Beer-Lambert law

$$A_i(\nu) = \exp\left(-\sum_j \int \alpha_j(\nu)\cdot dl\right) = \exp\left(-\sum_j \int \sigma_j(\nu)\cdot N\cdot dl\right), \quad (2)$$

where N is the number density of the absorbing gas, and $\sigma_j(\nu)$ is the absorption cross-section of the jth contributing transition to the absorption spectrum and is given by

$$\sigma_j(\nu) = S_j \cdot g_\nu(\nu-\nu_j), \quad (3)$$

where ν_j and S_j are the center frequency and the line strength of the jth absorption transition, respectively, and $g_\nu(\nu-\nu_j)$ is the corresponding line-shape function.

By discretizing the region of interest (ROI) into $N = n\times n$ square pixels as shown on the LHS of Fig. 1, Eq. (2) becomes

$$A_i(\nu) = \exp\left(-\sum_j \sum_k \sigma_j^k(\nu)\cdot N^k\cdot L_i^k\right), \quad (4)$$

where k is the index of one of the N pixels, $\sigma_j^k(\nu)$ is the absorption cross-section of the jth transition in the kth pixel, and N^k and L_i^k are the number densities of the absorbing gas and absorption path length of the probing beam within the kth pixel, respectively.

When a total number (I) of probing beams is available, the same number of MUMAS spectra can be measured. By sampling S points of the spectra that are represented as red dots on the right panel of Fig. 1, a total number of $S\times I$ nonlinear equations can be obtained with the distribution of temperature and absorbing species concentration as the variables. The nonlinear equation system can be formulated as

$$\begin{cases} P_1^m(\nu^1_{\rm scan}) = \sum_q W_q(\nu^1_{\rm scan})\cdot\left[1-\exp\left(-\sum_j\sum_k \alpha^c_{1,j,k}\right)\right] \\ \vdots \\ P_i^m(\nu^s_{\rm scan}) = \sum_q W_q(\nu^s_{\rm scan})\cdot\left[1-\exp\left(-\sum_j\sum_k \alpha^c_{i,j,k}\right)\right] \\ \vdots \\ P_I^m(\nu^S_{\rm scan}) = \sum_q W_q(\nu^S_{\rm scan})\cdot\left[1-\exp\left(-\sum_j\sum_k \alpha^c_{I,j,k}\right)\right], \end{cases} \quad (5)$$

where $P_i^m(\nu^s_{scan})$ is the measured signal of the ith beam at the scanned frequency of ν^s_{scan}.

The LHS of the equations are the measured MUMAS signals along various paths, and the RHS are the computed signals according to the model described above. The solution of the nonlinear equation system can then be cast into a minimization problem with a cost function as

$$F = \sum_{i=1}^{I}\sum_{s=1}^{S}\left(\frac{P_i^c(\nu^s_{\rm scan})}{P_i^m(\nu^s_{\rm scan})^{-1}}\right)^2, \quad (6)$$

where $P_i^c(\nu^s_{scan})$ is the calculated signal of the ith beam at the scanned frequency of ν^s_{scan}.

Additional *a priori* information such as the smoothness of distributions of temperature and species concentration can be incorporated into the cost function as

$$F = \sum_{i=1}^{I}\sum_{s=1}^{S}\left(\frac{P_i^c(\nu^s_{\rm scan})}{P_i^m(\nu^s_{\rm scan})^{-1}}\right)^2 + \gamma_T\cdot\|L\cdot\vec{T}\|^2 + \gamma_C\cdot\|L\cdot\vec{C}\|^2 = D + \gamma_T\cdot R_T + \gamma_C\cdot R_C, \quad (7)$$

where $\vec{T}$ and $\vec{C}$ are the fitted distributions arranged as column vectors; D is the residual in projections, which quantifies the difference between the fitted and measured projections; γ_T and γ_C are the weighting parameters employed to regulate the relative significance of *a priori* (smoothness) and *posteriori* (measured MUMAS signals) information; and L is the Laplacian matrix defined as

$$L_{ij} = \begin{Bmatrix} 1 & \text{if } i=j \\ -1/w & \text{if } j \text{ neighbors } i \\ 0 & \text{otherwise} \end{Bmatrix}, \quad (8)$$

where w is the total number of pixels neighboring the ith pixel.

The minimization problem can then be solved using a global optimization algorithm such as simulated annealing.[20]

Figure 2 illustrates how different flow parameters affect the MUMAS spectrum of a specific laser beam. Panel (a) shows four simulated spectra of water vapor with different temperatures by assuming a constant concentration, while panel (b) shows how the spectra change with respect to the species concentration when a constant temperature is assumed. Water vapor was chosen in this study since it is a major species of hydrocarbon/hydrogen flames, and also, a multi-mode interband cascade laser is now available to probe its signature

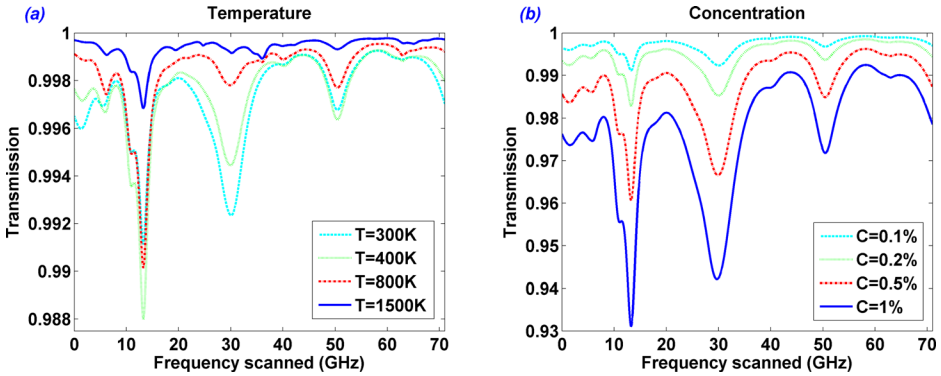

FIG. 2. Left panel (a): example MUMAS spectra of H_2O as a function of temperature when the species concentration assumed as constant; Right panel (b): example MUMAS spectra as a function of species concentration with the temperature assumed as constant. The center frequency is located at 5600 nm, and the mode space is around 70 GHz. The absorbing path length is 10 cm.

transitions. The HITRAN database was used in these simulations. As can be seen from panel (a), the strongest absorption feature remains almost the same as the temperature changes; however, the other absorption features change in a distinct way, indicating the nonlinear dependency of the MUMAS signal on temperature. On the other hand, the absorption features scale almost linearly as the concentration varies. The nonlinear dependency of the MUMAS spectra on temperature is the key factor underpinning the successful implementation of tomographic MUMAS.

To demonstrate the feasibility of tomographic MUMAS, extensive simulations were conducted. A variety of phantoms were tested in these simulations. Two representative phantom sets mimicking the multi-modal characteristics of practical flames are shown in the upper and bottom panels of Fig. 3, respectively. The region of interest (ROI) is discretized into 10×10 square pixels, resulting in a total number of 200 variables. It has been shown in the previous demonstration of nonlinear TAS based on multispectral absorption spectroscopy using either frequency-agile lasers or multiplexed single-mode diode lasers that, even when the inversion process leads to a poor concentration reconstruction, a faithful retrieval of temperature distribution is achievable. Due to the similar mathematical nature of tomographic MUMAS to the previous implementations of nonlinear TAS modalities, this conclusion should be still valid. This is indeed verified by the following numerical demonstrations in

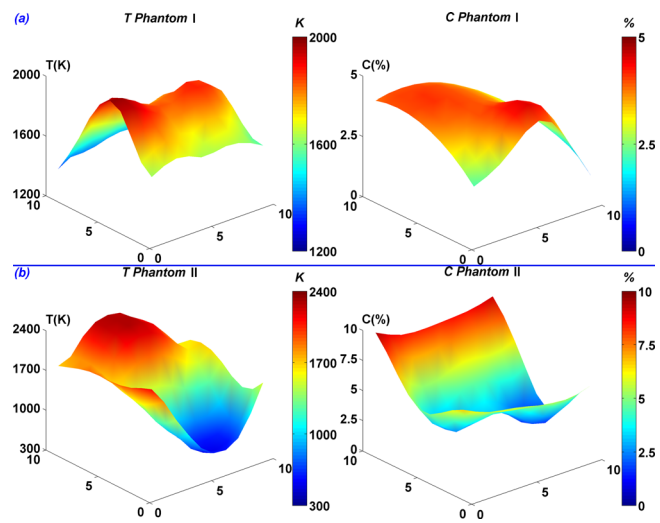

FIG. 3. Two phantom sets that are used for the simulation studies in this work, each containing phantoms of both temperature and species concentration.

which only the smoothness prior of temperature distribution is considered. To quantify the fidelity of temperature reconstruction, the averaged reconstruction error is defined here as

$$e_T = \frac{\sum_{m=1}^{M}\sum_{n=1}^{N} |T_{m,n}^{rec} - T_{m,n}^{true}|}{\sum_{m=1}^{M}\sum_{n=1}^{N} |T_{m,n}^{true}|}, \tag{9}$$

where $\vec{T}^{\text{rec}}$ and $\vec{T}^{\text{true}}$ are the reconstructed and ground truth distributions of temperature, respectively.

Panels (a) and (b) of Fig. 4 show the results from two simulated cases using the first phantom set. In these two cases, the ROI was probed using two orthogonal projections, with each containing 10 parallel beams. To simulate practical experimental conditions, 5% Gaussian noise was added to the projections (equivalent to a signal-to-noise ratio of 20). The inversion was conducted both with and without considering the smoothness prior of the temperature distribution. The reconstructions and the corresponding error contours are shown in panels (a) and (b), respectively. As can be seen, the case with the smoothness prior results in a smaller reconstruction error e_T and recovers the multi-modal feature of the phantom better. This results from a good balance between the *a priori* and *posterior* information. Such balance can only be achieved by setting a proper regularization parameter γ_T, the selection of which is non-trivial and will be discussed later.

Panels (c) and (d) of Fig. 4 are the counterparts of panels (a) and (b), respectively, but the results are from cases using the second phantom set, which features larger variations of both temperature and species concentration across the ROI. In the simulations, four projections each with 10 parallel beams were arranged in an equiangular manner. Again, 5% Gaussian noise is added to the projections. The larger variations in the phantoms cause more difficulties for the inversion process, as reflected by the increased reconstruction errors. By comparing e_T between these two cases, we can conclude that although the number of equations is larger than the number of variables, the inversion process only minimizing D cannot find a satisfactory solution. On the contrary, the smoothness regularization significantly improves the reconstruction quality. Thus, the incorporation of the *a priori* information is an effective way to increase the reconstruction fidelity whenever it is available.

As mentioned earlier, the regularization factor γ_T plays a critical role in the performance of the tomographic

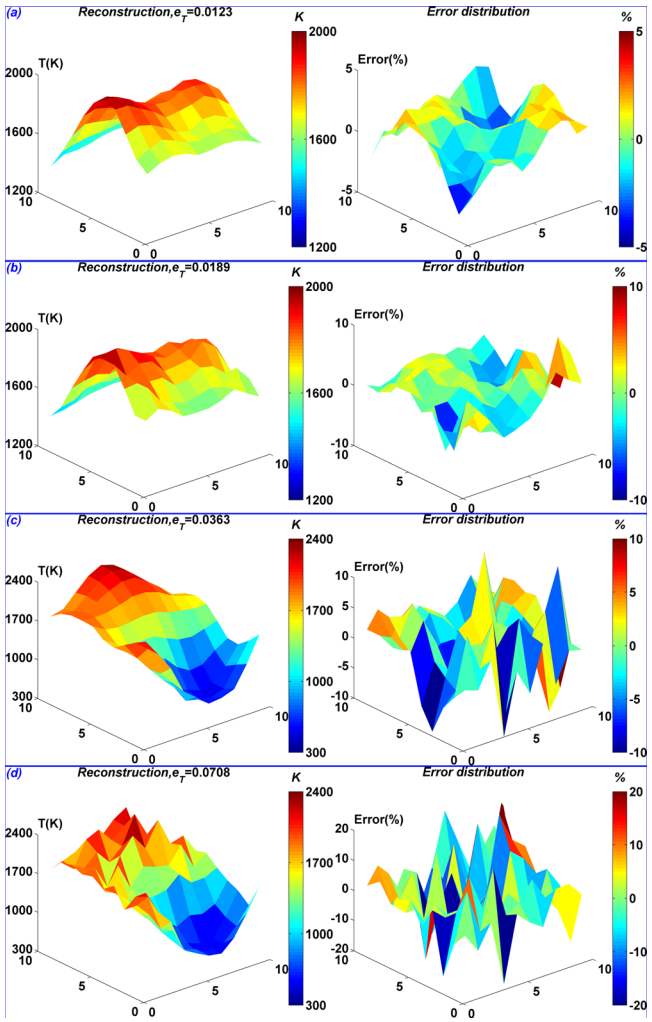

FIG. 4. Panel (a): the reconstruction and the error contours for the simulated case using the first phantom set with the smoothness prior assumed; Panel (b): the counterpart of Panel (a) but without the smoothness prior; and Panel (c) and (d): the counterparts of Panel (a) and (b) respectively but with the second phantom set used.

reconstruction. In real applications, the ground truth phantoms are unknown. Thus, optimal γ_T cannot be determined by referring to e_T obtained, as the latter is not available. Here, we propose a simple method to determine a near-optimal γ_T for a faithful reconstruction. Figure 5 shows how e_T, D, and $\gamma_T \times R_T$ evolve as a function of γ_T for the two regularized cases shown in Fig. 4. As can be seen from this figure, e_T nearly stays the same until a certain point and then becomes larger as γ_T increases. This is because when γ_T is small, the smoothness *prior* takes no effect and the SA algorithm only aims to guarantee the *posterior* information. On the other hand, when γ_T is large, the solution will be over-smoothed and D is not guaranteed to be a minimum. The optimal γ_T occurs at the point right before D starts to increase. This phenomenon exactly agrees with the previous reasoning that the optimal γ_T should minimize D and at the same time satisfy the *a priori* information as much as possible.

Even though this work mainly focuses on the thermometry, it has to be pointed out that when the temperature distribution is recovered and re-inserted into Eq. (6), the concentration map may also be recovered since the only

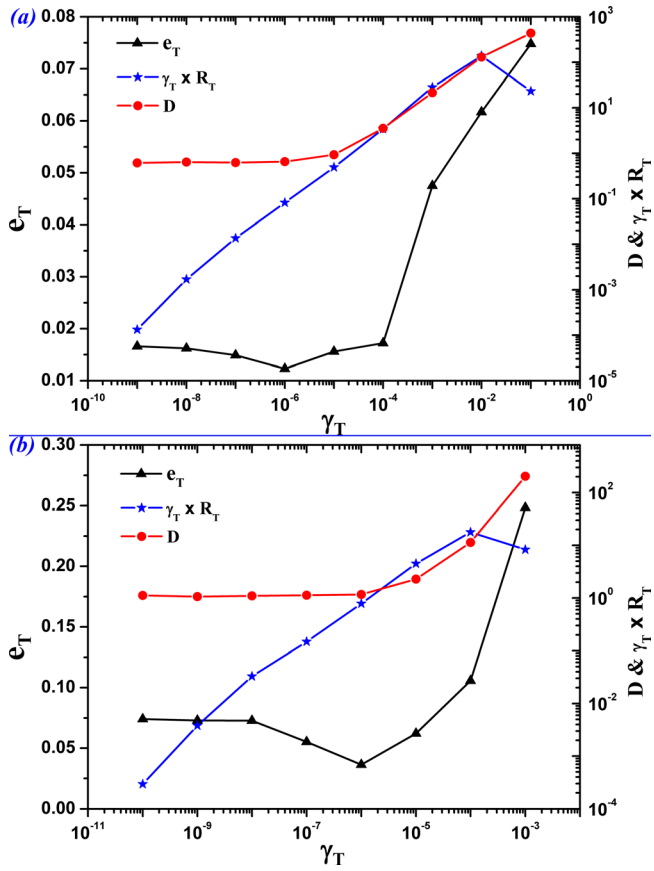

FIG. 5. Panel (a): the evolution of e_T, D, and $\gamma_T \times R_T$ as a function of γ_T for the case shown in Panel (a) of Fig. 4; and Panel (b): the counterpart of Panel (a) but for the case shown in the Panel (c) of Fig. (4).

variables will be the distribution of concentration, and Eq. (6) becomes a linear equation system, which can be solved using the well-established classical tomographic algorithms such as the algebraic reconstruction technique[3] and the Landweber algorithm.[21] Readers are referred to previously published work for more details of linear modalities of TAS.

To summarize, this work proposed a hyperspectral tomographic technique by combining the concept of nonlinear tomography and multi-mode absorption spectroscopy. Compared with the previous implementations of nonlinear tomographic absorption spectroscopy, this modality features critical advantages such as the availability of laser sources for a broad spectral range, cost-effectiveness compared with other broadband sources, and the capability to probe multiple flame species. The proof-of-concept numerical studies conducted in this work verified its feasibility and robustness for spatially resolved flame thermometry. The same capability to determine temperature and concentration distributions using tomographic MUMAS could also find applications in environmental monitoring, leak detection in industrial or waste disposal facilities, etc. Work is in progress to experimentally demonstrate the potential of this technique. In addition, the spectral range selected here was not optimized to achieve the best temperature sensitivity for a specific temperature range. However, even in the example spectra shown in Fig. 2, different features of the MUMAS spectrum display different temperature sensitivities. Thus, development of an effective method to select the optimal spectral range for a

temperature range of interest is one of our next research topics.

This work was funded by the Chinese Government "Thousand Youth Talent Program" and the National Science Foundation of China under Grant No. 51706141 and by the Engineering and Physical Sciences Research Council (EPSRC) UK under Grant No. EP/K029460/1.

[1]C. Liu, L. Xu, J. Chen, Z. Cao, Y. Lin, and W. Cai, Opt. Express **23**(17), 22494 (2015).
[2]W. Cai and C. F. Kaminski, Prog. Energy Combust. Sci. **59**, 1 (2017).
[3]T. Yu and W. Cai, Appl. Opt. **56**(8), 2183 (2017).
[4]T. Yu, B. Tian, and W. Cai, Opt. Express **25**(6), 5982 (2017).
[5]F. Wang, Q. Wu, Q. Huang, H. Zhang, J. Yan, and K. Cen, Opt. Commun. **346**, 53–63 (2015).
[6]S. A. Tsekenis, N. Tait, and H. McCann, Rev. Sci. Instrum. **86**(3), 035104 (2015).
[7]W. Cai and C. F. Kaminski, Appl. Phys. B **119**(1), 29–35 (2015).
[8]W. Cai and C. F. Kaminski, Appl. Phys. Lett. **104**(3), 034101 (2014).
[9]W. Cai and C. F. Kaminski, Appl. Phys. Lett. **104**(15), 154106 (2014).
[10]L. Ma, X. Li, S. T. Sanders, A. W. Caswell, S. Roy, D. H. Plemmons, and J. R. Gord, Opt. Express **21**(1), 1152 (2013).
[11]Y. Arita, P. Ewart, R. Stevens, K. Richard, and P. Manson, in *Proceedings of the 4th Australian Conference on Laser Diagnostics in Fluid Dynamics and Combustion* (2005), pp. 9–12.
[12]A. Thompson, H. Northern, B. Williams, M. Hamilton, and P. Ewart, Sens. Actuators, B **198**, 309 (2014).
[13]S. O'Hagan, T. Pinto, P. Ewart, and G. A. D. Ritchie, Appl. Phys. B **122**(8), 226 (2016).
[14]J. H. Northern, S. O'Hagan, B. Fletcher, B. Gras, P. Ewart, C. S. Kim, M. Kim, C. D. Merritt, W. W. Bewley, and C. L. Canedy, Opt. Lett. **40**(17), 4186 (2015).
[15]S. O'Hagan, J. H. Northern, B. Gras, P. Ewart, C. S. Kim, M. Kim, C. D. Merritt, W. W. Bewley, C. L. Canedy, and I. Vurgaftman, Appl. Phys. B **122**(6), 173 (2016).
[16]H. Northern, S. O'Hagan, M. L. Hamilton, and P. Ewart, Appl. Phys. B **118**(3), 343 (2015).
[17]M. L. Hamilton, G. A. D. Ritchie, Y. Arita, and P. Ewart, Appl. Phys. B **100**(3), 665 (2010); J. H. Northern, A. W. J. Thompson, M. L. Hamilton, and P. Ewart, *ibid.* **111**(4), 627 (2013).
[18]Y. Arita, R. Stevens, and P. Ewart, Appl. Phys. B **90**(2), 205 (2008).
[19]Y. Arita and P. Ewart, Opt. Commun. **281**(9), 2561 (2008).
[20]W. Cai and L. Ma, Comput. Phys. Commun. **181**(1), 11 (2010).
[21]H. Liu, T. Yu, M. Zhang, and W. Cai, Appl. Opt. **56**(25), 7107–7115 (2017).